ELSEVIER

Contents lists available at ScienceDirect

Journal of Water Process Engineering

journal homepage: www.elsevier.com/locate/jwpe





Double-layer magnetized/functionalized biochar composite: Role of microporous structure for heavy metal removals

Baharak Sajjadi ^{a,*}, Ronish M. Shrestha ^a, Wei-Yin Chen ^a, Daniell L. Mattern ^b, Nathan Hammer ^b, Vijayasankar Raman ^c, Austin Dorris ^b

- a Department of Chemical Engineering, School of Engineering, University of Mississippi, 134 Anderson Hall, MS 38677-1848, USA
- ^b Department of Chemistry and Biochemistry, University of Mississippi, Coulter Hall, MS 38677, USA
- ^c National Centre for Natural Products, School of Pharmacy, University of Mississippi, University, MS 38677, USA

ARTICLE INFO

Keywords: Biochar Ultrasound activation Magnetization Adsorption Heavy metal Water treatment

ABSTRACT

Magnetization facilitates the separation and reuse of adsorbents, but significantly reduces the adsorption capacity. In this study, a double layer magnetized/functionalized biochar composite was synthesized through a hybrid post-pyrolysis magnetization which sustained and even significantly increased the adsorption capacity of microporous carbonaceous biochar (BC). The developed process included i) structural modification of biochar under ultrasound waves, ii) magnetization with magnetite (Fe₃O₄) nanoparticles, and iii) functionalization with 3-aminopropyltriethoxysilane (TES). Ultrasound irradiation exfoliates and breaks apart the irregular graphite layers of biochar, and creates new, or opens blocked, micropores, thus enhancing the BC's porosity. For its part, TES stabilizes the magnetic nanoparticles on the biochar surface, while it participates in water decontamination through the strong chelation ability of its amino groups toward metal ions. Scanning electron microscopy demonstrated the stable and uniform distribution of Fe₃O₄ nanoparticles on the surface of microporous biochar, and Fourier-transform infrared spectroscopy indicated effective surface functionalization. In addition, although magnetization usually reduces the porosity of carbonaceous adsorbents, the ultraviolet-visible spectroscopic analysis showed that double layer magnetic biochar composite exhibited a much greater ability to remove Ni(II) and Pb(II), with 139 % and 38 % higher adsorptions than raw biochar. Almost complete removal of Pb (91 %) was observed by magnetic-BC and the adsorbent could easily be separated using a neodymium magnet. This high performance can be attributed to the synergistic effect of ultrasound activation on increasing the porosity and surface area of biochar along with enhanced chelation imparted by amine functionalization. The developed technique can be used for synthesizing advanced adsorbents for removal of nuclear waste-related metal ions from aqueous environments.

1. Introduction

Owing to the rapid boom in industrialization, the proper treatment of the heavy metals from industrial wastewater has become of monumental importance [1]. Heavy metals are readily soluble in aquatic environs and once these connect up to food or drinking water chain, considerable concentrations can accumulate inside the human body which can be lethal if allowed to go beyond tolerable limits [2,3]. Nickel and lead, which are used in manufacturing processes of batteries, super-alloys, and smelting of sulfide ores, are considered to be severely toxic even at low concentrations. In addition to such common metal ions, efficient removal of toxic nuclear waste-related metal ions, is another important

application of adsorbents from the environmental standpoint. Biosorbents and activated carbons are good adsorbents for these metal ions but compared to biochar (BC), are relatively expensive. Biochar, the solid byproduct of biomass pyrolysis, with a microporous carbonaceous structure, has been increasingly recognized as an efficient adsorbent for a vast number of pollutants. Surface area, porosity and functionality of biochar govern the sorption capacity and the sorption mechanisms involved. Generally, pore size and the surface area tends to increase with pyrolysis temperature. The dehydration process due to water loss during pyrolysis generates pores of different sizes of nano (<0.9 nm), micro (<2 nm), and macro (>50 nm). Regardless of their charges or polarity, biochar with relatively small pore size is inefficient in trapping large

E-mail address: bsajjadi@olemiss.edu (B. Sajjadi).

^{*} Corresponding author.

sorbates [4]. In general, the micro- and mesopores are more important in the removal of metal ions [5]. In addition, the application performance of biochar is closely related to the quantity and types of functional groups. The three N-functional groups, Pyrrolic-N, pyridinic-N and graphitic-N are related to catalysis of oxygen reduction while amine-N influenced the adsorption of metal ions and CO₂. Therefore, better performance is corresponding to the abundance of active N-functional groups and the increase in the nitrogen content of biochar [6]. Surface amination is among the most common methods to introduce amino groups into biochar. The addition of basic amino groups to the surface is a promising method for increasing the efficiency of biochar in adsorption of carbon dioxide and metal ions. To reach this objective, three different methods can be applied: surface amination through I) nitration by ammonia, II) nitration by amino-containing reagents, III) combination of nitration and reduction [7].

A hindrance to these ongoing advancements in metal ion adsorption has been biochar recovery after wastewater treatment. Time-consuming steps like centrifugation and filtration are unlikely to be efficient in large scale applications. The magnetization of biochar has provided a novel approach, allowing practical use of small particle size adsorbents which have high surface areas and fast adsorption kinetics. High performance, magnetically separable adsorbent is also a readily applicable technology, which would reduce the harmful impacts of nuclear waste-related metal ions and radioactive material on human health and the environment; e.g. Fukushima Daiichi nuclear disaster after a 9.0 magnitude earthquake on March 2011, in which large amounts of water were contaminated with radioactive isotopes. With the use of a magnet, magnetic biochar can be easily and quickly separated after adsorbing heavy metal contaminants from water. This makes either batch or stirred processes a viable option while also overcoming the drawbacks caused by filtration of small particle size adsorbents and delivering faster adsorption kinetics [8]. Magnetic biochar can also effectively be used in the removal of inorganic anions, antibiotics, pesticides, organic dyes, nuclear materials and other organic pollutants from aqueous solution or wastewaters [9,10].

Impregnation, co-precipitation, and liquid reduction are the most common methods that have been used to prepare magnetic biochar. Impregnation includes mixing the biomass with a ferric or ferrous chloride precursor solution, and subsequent pyrolysis of the obtained biomass in an inert environment under high temperature. This singlestep pyrolysis of FeCl3-loaded biomass can produce biochar with magnetic properties but simultaneously produces secondary pollution, is costly and may not address any desired functional group on biochar surface [11]. Liu et al. [12] developed a Fe₃O₄-loaded magnetic biochar, with a spinel structure (magnetite, Fe₃O₄ or maghemite, γ-Fe₂O₃) using a mixture of FeCl₃ and biomass in a pyrolysis process under the flow of nitrogen, N2 gas at 600 °C for almost 3 h. The composite, exhibiting a large surface area of 349 m²/g and was effective for As(V) adsorption. A similar method has been used by other researchers to produce well-crystallined magnetic biochar [13,14]. However, surface functional groups which support adsorption through complexation become limited via this process as they react with iron in various oxidation reactions during pyrolysis, reducing biochar's heavy metal adsorption capacity significantly [15,16]. The magnetization of biochar has typically been achieved through the traditional method of chemical co-precipitation with magnetite (Fe₃O₄) [15,17]. In this process, iron oxides of magnetic nature are precipitated directly onto the biochar with the use of biocarbon and a mixed Fe²⁺/Fe³⁺ salt solution. These iron compounds have been used individually or in unison to impart magnetism on the biochar [18,19]. The liquid-phase reduction method comprises mixing the biocarbon with Fe²⁺ salt solution and then reducing Fe²⁺ to zero-valent iron on the biochar surface using a reducing agent (NaBH₄/KBH₄). Philippou et al. [20] investigated the fabrication of magnetic biochar (pncm) and Fe₃O₄-loaded oxidized biochar (pncom) using pine needles as a precursor in a co-precipitation process. The results showed better adsorptive properties for pncom, particularly in the acidic pH range.

However, the co-precipitation and liquid-phase reduction can reduce the porosity of biochar due to the aggregation of iron oxides in the aqueous solution. This results in a decrease in the surface area and hence the adsorption capability of biochar [21]. Even with the optimum amount of doping, the decrease in heavy metal adsorption is prevalent. To reap the benefits of magnetic separation, overcoming these drawbacks is crucial [22]. Recently more complicated magnetic biochar structures have been synthesized using electrostatic attraction. Cui et al. [23] developed a core-shell γ-Al₂O₃/Fe₃O₄ biochar (AFBC) through electrostatic attraction and inner-sphere complexation. AFBC represented a high phosphorus recovery and excellent stability. Nanoscale colloidal iron oxide (Fe₃O₄) nanoparticles (NPs) that exhibit superparamagnetic properties at ambient temperatures can deliver magnetic property to the carbonaceous structures. However, bare Fe₃O₄ nanoparticles are easily aggregated and reduce the porosity if they are directly precipitated on carbon structure [24]. The Fe₃O₄ NPs may also be detached once the adsorbent comes in contact with water. In order to overcome these drawbacks, a homogenous loading and immobilization of magnetic nanoparticles on/into carbon structure has been regarded as an efficient method to increase the stability of NPs, yet, delivering the magnetic property while the original porosity of the structure is also maintained. To reach these objectives physical activation of carbon structure using ultrasound waves and simultaneous immobilization-functionalization is proposed in this research work.

This study proposes a novel magnetization process to synthesize a double-layer functionalized magnetic biochar composite (TES/Fe₃O₄/ biochar) through a three-step process: I) physical activation of biochar under ultrasound irradiation (US-BC), II) magnetization of sonoactivated biochar with Fe₃O₄ nanoparticles (USMBC) and III) functionalization of USMBC with 3-(triethoxysilyl)propylamine (TES). Activating biochar (BC) with ultrasound (US) irradiation, which include disarrangement and exfoliation of BC's graphitic structure, mineral leaching and a significant increase in BC's porosity, significant increase in BC's internal surface area, creation of new and opening of blocked mesopores, and enhanced carbon and hydrogen content of biochar [25]. All these phenomena provide more room for magnetic nanoparticles, functional groups and subsequently adsorption capacity. TES improve the stability of Fe₃O₄ nanoparticles (Fe-NP) on the biochar surface and increase adsorption sites (functional groups) for heavy metals. The process suggested not only facilitates biochar removal after heavy metal adsorption but also increases its adsorption capacity. This study investigates the synergisms of ultrasound activation, Fe₃O₄ loading, and TES functionalization with respect to adsorption rates of nickel and lead.

2. Materials and methods

2.1. Materials

Commercial Pinewood biochar supplied by Biochar Now (Berthoud Colorado, U.S.A) was used for the purpose of this experiment. The biomass is pyrolyzed at a temperature between 550 and 600 °C in a kiln reactor with a multi-zone combustion chamber for 8 h, after which nitrogen is introduced to discontinue the process. The reagents used in the magnetization process were iron(III) chloride (FeCl $_3$, 97 % purity), iron (II) sulfate heptahydrate (FeSO $_4$.7H $_2$ O, 99.0 % purity), 3-(triethoxysilyl) propylamine (TES) and ammonium hydroxide (NH $_4$ OH, 28 % NH $_3$ in H $_2$ O, 99.0 %), all of which were obtained from Sigma Aldrich. The chemicals for preparing stock heavy metal solutions, Lead (II) Chloride (98 % purity) and Nickel (II) Chloride (98 % purity), were also obtained from Sigma Aldrich. The standards used for the measuring heavy metal concentration, TNT856 for Nickel and TNT850 for Lead, were purchased from Hach.

2.2. Experimental method

2.2.1. Ultrasound treatment of Biochar and magnetization

The raw biochar was first ground in a ball mill grinder and sieved several times to the range of $75-125 \,\mu m$. To modify the physical structure, a mixture of biochar in water (7.5 g in 250 mL) was irradiated with low-frequency ultrasound (OSonica sonicator model No. Q700, max power 700 W) [26]. The duration of ultrasound treatment was selected based on the optimum values (30 and 60 s) obtained from our previous studies [26,27] (Fig. 1a). Iron (III) chloride (FeCl₃) and iron (II) sulfate heptahydrate (FeSO₄.7H₂O) with a 2:1 M ratio were dissolved in pre-degassed distilled water. The solution was stirred for 30 min at room temperature. NH₄OH 28 % with an amount sufficient to balance Fe²⁺ + $2Fe^{3+} + 8OH^{-} \rightarrow Fe_3O_4 + 4H_2O$ (in other words, $FeSO_4 + 2FeCl_3 +$ $8NH_4OH^- \rightarrow Fe_3O_4 + 6NH_4Cl + (NH_2)SO_4 + 4H_2O$ was then dropwise added to precipitate the iron(II,III) oxide (Fe₃O₄) nanoparticles and the mixture was kept stirring for 5 h at 80 °C [28] (Fig. 1b). All these syntheses were performed in an inert atmosphere (N2) in a glove box to avoid uncontrolled oxidation and formation of non-magnetic oxides through oxidation of Fe²⁺ to Fe³⁺, giving higher yield of magnetite particles. The black precipitate was collected by filtration, washed with 100 mL distilled water several times until the pH was brought down close to 7 and dried under vacuum at 60 °C for 12 h [28]. In the next step, varying ratios of ultrasono-activated biochar (US-BC) and iron(II, III) oxide nanoparticles (1:1, 2:1, and 3:1) were mixed with distilled water and stirred for 2 h at 50 °C to obtain Fe $_3$ O $_4$ -loaded biochar (Fig. 1c). The ultrasono-magnetized biochar was then subjected to chemical functionalization with 3-aminopropyltriethoxysilane (TES) [29,30]. The dried composite of Fe $_3$ O $_4$ -loaded biochar (6 g) in 150 mL of water was treated with TES (5, 10 or 15 mL) and stirred for 8 h at 50 °C (Fig. 1d). Eventually, the functionalized-magnetized biochar composite was filtered, washed with distilled water several times (until pH was close to 7) and dried at 60 °C for 12 h.

2.2.2. Characterizations of the adsorbent

The porosities and surface areas of the raw, ultra-sonicated, and magnetized biochars were measured using a surface area analyzer (3Flex MicroActiveTM Share Multiport Surface Characterization Analyzer, 350/00,001/00EDU). Prior to analysis, the samples were degassed at 373 K for 3 h. The analysis was done with a liquid nitrogen bath at 77 K and the technique measures volume adsorbed by the sample as the relative pressure is gradually increased from 0 to 1. Then, the mesopore area and pore volume were calculated by the BET (Brunauer, Emmett and Teller) equation. The t-plot based on the de-Boer equation was also used to calculate micropore surface area and pore volume [31]. The morphological analysis was conducted using SEM (JSM-5600

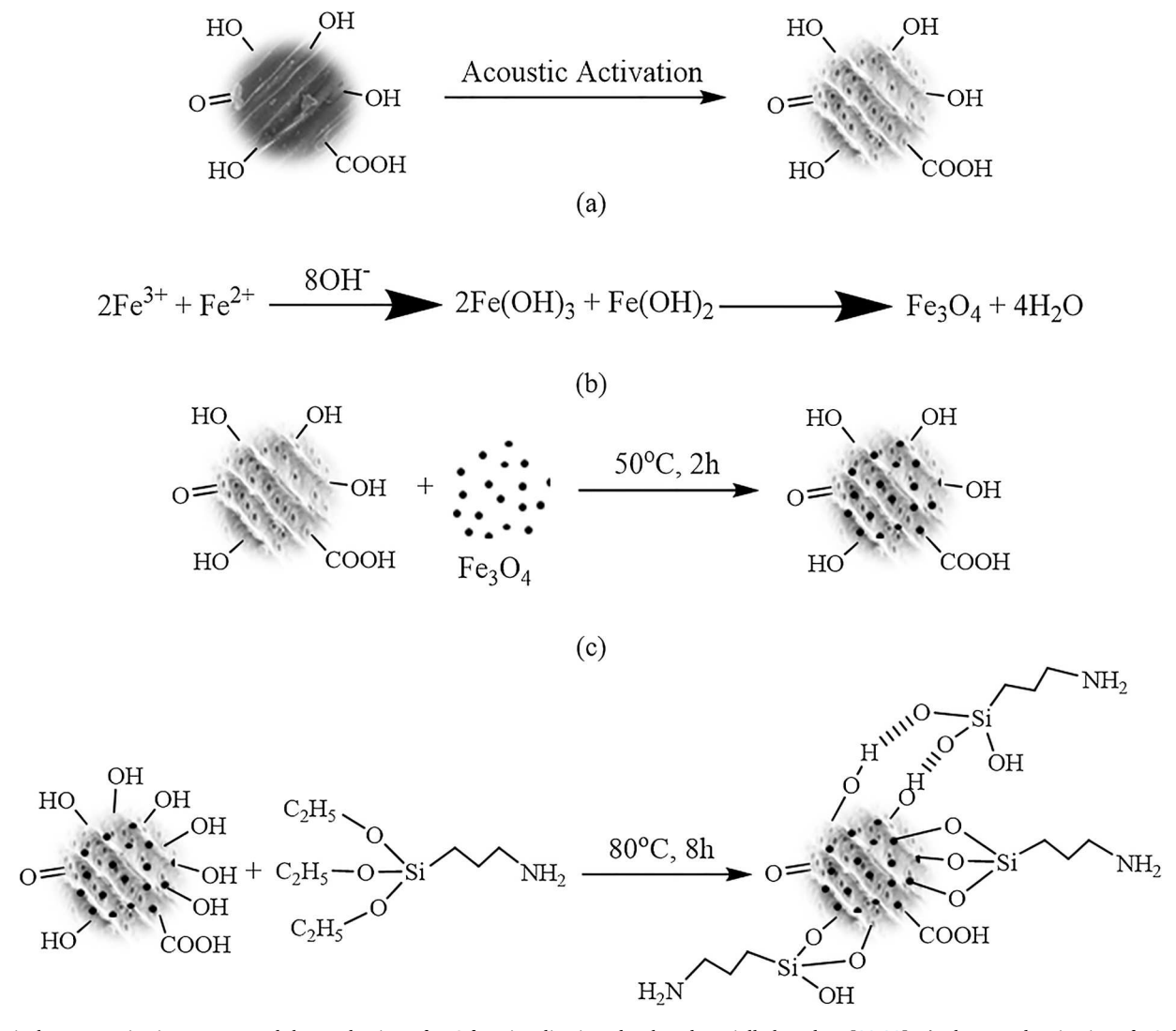


Fig. 1. Biochar magnetization process and the mechanism of TES functionalization, developed partially based on [29,30], a) Ultrasound activation of BC, b) Fe_3O_4 synthesis, c) BC magnetization, d) TES functionalization.

Scanning Electron Microscope, JEOL USA Inc., Peabody, MS) at an accelerating voltage of 5-7 kV using a JSM-5600 SEM (JEOL Ltd., Tokyo, Japan). The samples were mounted on aluminum stubs using glued carbon tapes and then coated with platinum for 3 min. at about 120 mTorr pressure using a Hummer 6.2 sputter coater (Anatech USA, Union City, CA, USA). The sputter coater chamber was supplied with argon gas during the coating process. The presence of iron and organic elements (C, N, H, O) was investigated through combustion analysis by Huffman Hazen Laboratory, Colorado, USA. Fourier Raman (LabRam HR Evolution, USA). Fourier Transform Infrared (FTIR, Cary 660 FTIR Agilent, USA) spectroscopies were also employed to characterize the graphitic structure of samples and surface functional groups, the doping of iron oxides on the biochar surface and the presence of TES. Raman spectra were acquired in the air at room temperature using a 532-nm wavelength laser. The laser was focused onto the sample using a 100X objective. For FTIR analysis, samples were dried at 333 K under vacuum prior to analysis. A background scan was conducted before each sample is scanned. Samples were put in ATR crystal and scanned in the wavelength range of $400-4000 \text{ cm}^{-1}$.

2.2.3. Nickel and lead adsorption studies

Distinct solutions containing 100 mg/L Ni $^{2+}$ and Pb $^{2+}$ were prepared using powdered nickel (II) chloride (98 %, Sigma Aldrich) and powdered lead (II) chloride (98 %, Sigma Aldrich), respectively. In each adsorption experiment, 0.5 g of the synthesized biochar composite was added to a 50 mL solution of 100 mg/L Ni $^{2+}$ or Pb $^{2+}$ and was stirred in a shaker for

varying durations (30 min, 1, 2, 4, and 6 h), after which the biochar was separated from the solution, first using strong neodymium magnets (Fig. 2a) and further by filtration. The metal ion concentration of the filtrate was determined through UV–vis spectroscopy (DR6000, Hach) using the respective standard kits (TNT856 for nickel using Dimethylglyoxime Method and TNT850 for lead using PAR method). For the former, nickel ions react with dimethylglyoxime in an alkaline solution to form an orange-brown complex. The measurement wavelength is 463 nm. In the latter, lead (II) ions react at pH 9 with 4-(2-pyridylazo)-resorcinol (PAR) to form a red complex. The measurement wavelength is 520 nm. Metal concentrations were greater than the measuring range. Therefore, the samples were first diluted with distilled water to prevent precipitation in the vial.

2.2.4. Kinetic studies

The equilibrium adsorption capacities for Ni(II) and Pb(II) were calculated according to $q_e = \frac{(C_0 - C_e)V}{M}$, where C_0 , C_e , V and M are the initial and the residual concentration of metal ions in the solution (mg. L^{-1}), the volume of heavy metal solution (mL) and the amount of adsorbents (mg), respectively. In addition, both the pseudo-first-order $\left(\ln(q_e - q_t) = \ln q_e - k_1 t\right)$ and pseudo-second-order $\left(\frac{t}{q_t} = \frac{1}{k_2 q_e^2} + \frac{1}{q_e} t\right)$ equations were used to model the adsorption kinetics, where q_t and q_e

equations were used to model the adsorption kinetics, where q_t and q_e (mg/g) are the amount of metal ion adsorbed per gram of adsorbent at time t and at equilibrium, respectively. k_1 (min⁻¹) and k_2 (g/(mg min) are the rate constants for the pseudo-first-order and pseudo-second-

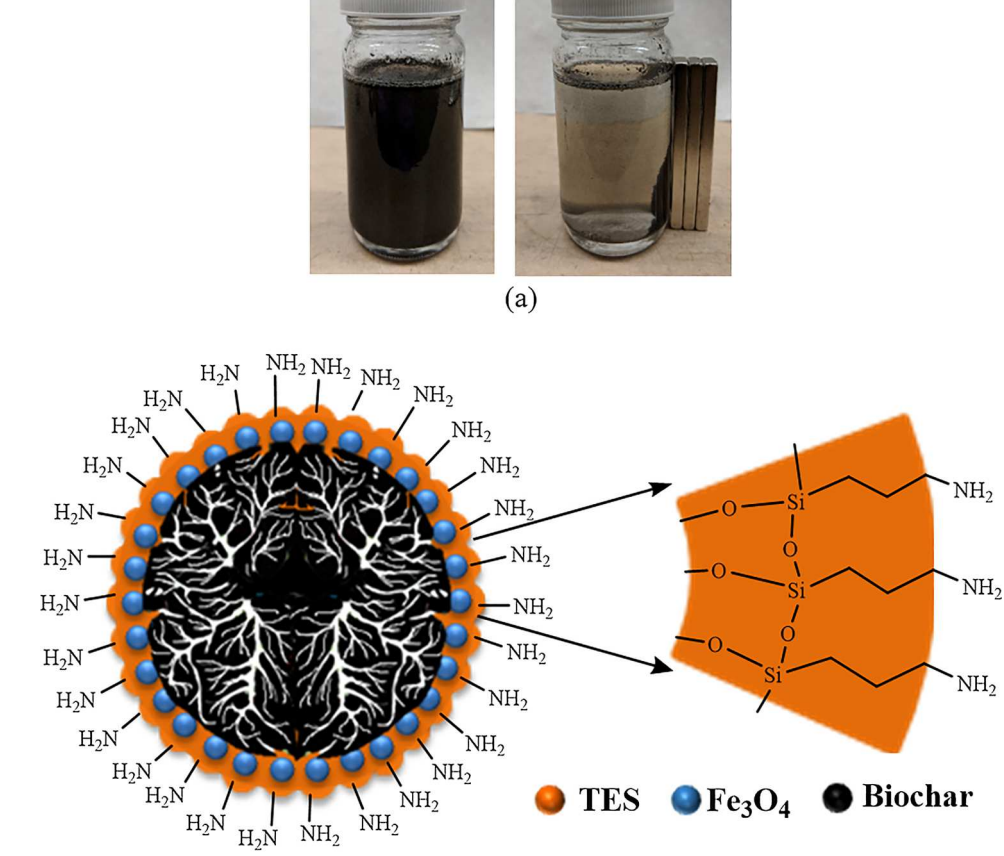


Fig. 2. a) Separation of 0.5 g biochar in 50 mL water by a neodymium magnet, b) A schematic diagram of the silica network on the surface by Si-O-C and Si-O-Si bonds.

(b)

order adsorption models, respectively.

3. Results and discussion

3.1. Mechanism of chemical activation of Biochar-NP with TES

The co-precipitation process has a well-known mechanism as represented by Eq. (1-3). This process can synthesize nanoparticle sizes in the range above 10 nm.

$$Fe^{2+} + 2OH^{-} \rightarrow Fe(OH)_{2} \tag{1}$$

$$Fe^{3+} + 3OH^{-} \rightarrow Fe(OH)_{3}$$
 (2)

$$Fe(OH)_2 + 2Fe(OH)_3 \rightarrow Fe_3O_4 + 4H_2O$$
 (3)

Though loading the magnetic Fe_3O_4 on the surface (Fig. 3def) delivers magnetization properties to the biochar matrix, some magnetic nanoparticles may be detached when the biochar comes in contact with aqueous solutions. The main objectives of TES addition include stabilizing the Fe_3O_4 nanoparticles (Fe-NP), preventing the dissociation of

Fe-NPs from the biochar thereby improving the reusability of the adsorbent, and increasing the quantity of nitrogen-containing functional groups for enhanced adsorption of metal ions (Fig. 2b). TES can be attached to the porous structure of biochar either through impregnation using weak van der Waals forces [32] or grafting using strong covalent bonds to the biochar's functional groups. Theoretically, surface functionalization with TES should afford a homogeneous coupling as surface OH groups replace the ethoxy groups on TES (Fig. 2b) [29,30]. However, hydrogen bonding between surface OH and silanols/amino groups may also happen (Fig. 1) [30].

The amine functional groups of TES can increase the adsorption capacity due to complexation with heavy metals [7,33]. Cu(II), Ni(II) and Pb(II) strongly bind to amine groups. Weaker binding has been observed between amine-containing sites and Cd(II) or Zn(II). However, they still prefer amine sites to pure carboxylates. No preference has been observed for Ca(II) binding with amine compared to carboxylate ligand groups, indicating Ca(II) is bound by more negatively charged molecules [34]. Amine groups also effectively participate in the adsorption of Cr (VI). Amination with 3-aminopropyltrimethoxysilane (APTMS), which is analogous to TES, increases the Cr(VI) uptake of mesoporous silica

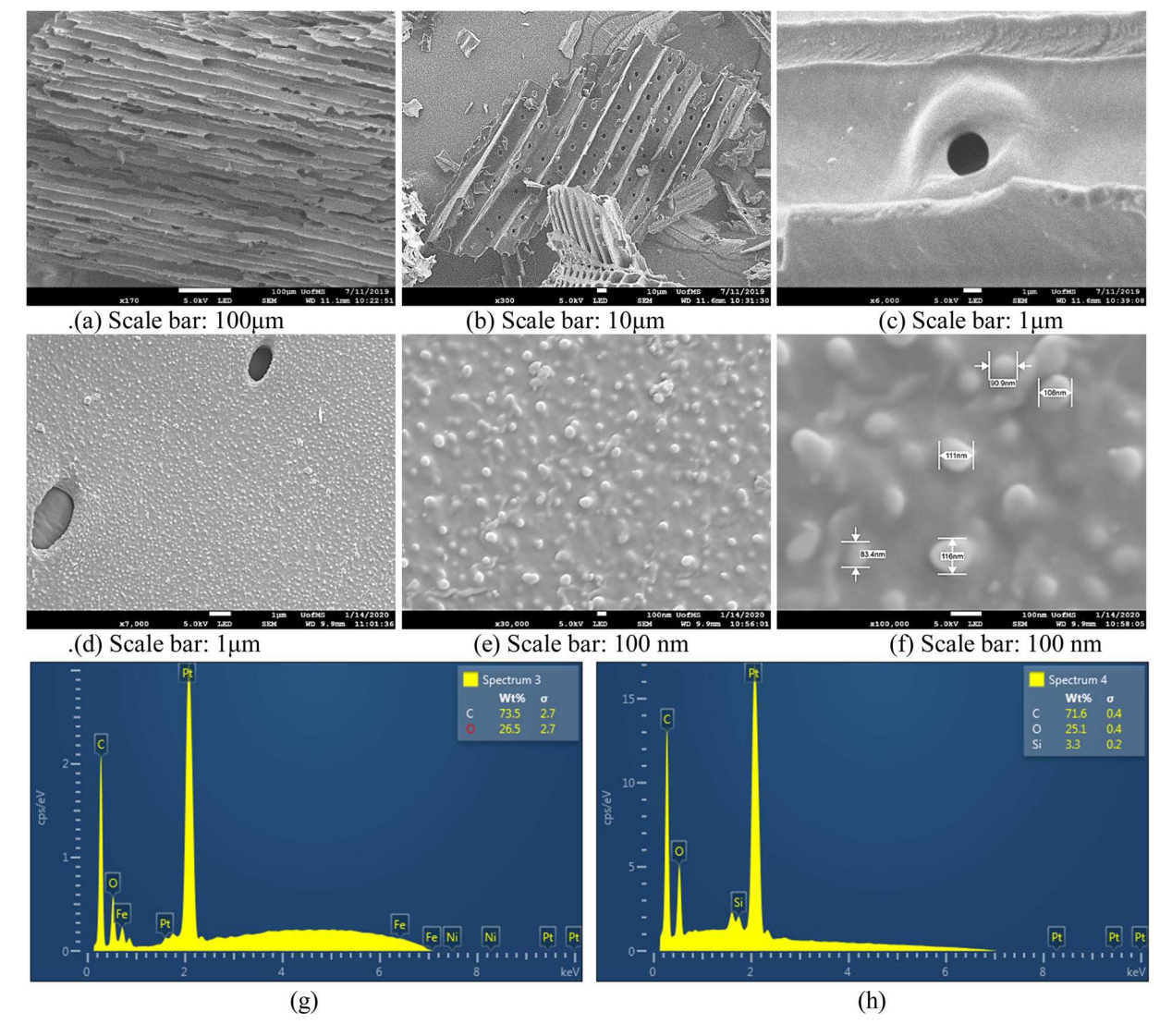


Fig. 3. SEM images of (a) raw biochar (longitudinal view), (b) ultrasound activated biochar, (c) ultrasound-generated pore with a diameter of 2 μm, (d, e, f) magnetized and functionalized surface. EDX analysis of (g) magnetized and (h) magnetized and functionalized biochar. Note 1: The longitudinal structure of raw biochar does not contain any pores; all well-ordered pores were generated by ultrasound physical activation. Note 2: Figures c and d both are of the same scale, clarifying the distinction between the smooth surface of ultrasound-activated biochar before magnetization and its rough surface after magnetization and functionalization. Note 3: Images g and h demonstrate the elemental percentage composition C, O, Fe and Si on the surface of the magnetized and functionalized biochar.

from 36.95 mg/g to 83.50 mg/g [35]. Bamdad et al. [29] applied two different chemical methods for amine functionalization of biochar, including i) nitration using concentrated nitric acid, followed by reduction, and (ii) condensation of TES on the surface. Though the authors concluded that a moderate thermal activation is needed after amination, TES-aminated biochar indicated a higher CO_2 adsorption capacity compared to nitration-reduction.

3.2. Physical activation of biochar

Table 1 shows the surface area and total pore volumes of raw, ultrasound activated and magnetized/functionalized biochars using different loadings of Fe-NP and TES concentrations. The specific surface area of BCs was calculated using the Brunauer-Emmett-Teller (BET) and Harkins and Jura Equations. The impact of ultrasound activation on increasing the micro-porosity and surface area of BC has recently been proved as an effective method for the physical activation of biochar. This effect is mainly attributed to ultrasound-induced cavitation and its implications. In addition, the explosion of cavitation bubbles and generation of micro-jets can create a regular pattern of new pores into/onto the biochar surface which is visible in SEM images (Fig. 3b vs a). As a result, the BET surface area of raw biochar increased from 219.98–261.67 m²/g after only 30 s of BC exposure to ultrasound irradiation. On the other hand, the mesopore surface area reduced from $96.54-68.45 \text{ m}^2/\text{g}$ due to the partial conversion of mesopores to micropores. In other words, many macropores are broken down into micropores enhancing the overall surface with more porosities. As expected, the loading of nanoparticles and TES functionalization reduced micro and mesoporosity of biochar and lowered its surface area by 13 %, which may cause a reduction in the adsorption capacity, yet exposure to 60 s of ultrasound activation could sustain much of the BET surface area when BC was magnetized and functionalized, with a loss of only 2 % compared with raw BC. Further porosity reduction was observed by increasing the concentration of TES or maximizing the loading of nanoparticles. Accordingly, the minimum

Table 1
Surface area and porosity of raw and magnetized biochars.

ID	BET Surface Area (m ² / g)	Using Harkins and	t-plot		
		t-plot Micropore Surface Area (m²/g)	t-plot Mesopore Surface Area (m²/g)	Micropore Volume (cm ³ / g)	
Raw BC	219.98	123.44	96.54	0.0458	
US30	261.67	193.22	68.45	0.0575	
US 0 BC:	190.88	112.23	78.65	0.0504	
Fe-2:1					
TES5					
US30 BC:	197.10	138.67	58.43	0.0563	
Fe-2:1					
TES5					
US60 BC:	214.86	155.43	59.43	0.0533	
Fe-2:1					
TES5					
US30 BC:	182.15	118.71	63.44	0.0349	
Fe-1:1					
TES5					
US30 BC:	197.10	138.67	58.43	0.0563	
Fe-2:1					
TES5					
US30 BC:	200.93	118.44	82.49	0.0525	
Fe-3:1					
TES5					
US30 BC:	197.10	138.67	58.43	0.0563	
Fe-2:1					
TES5					
US30 BC:	201.45	148.76	52.69	0.0379	
Fe-2:1					
TES10					
US30 BC:	181.65	125.98	55.67	0.0335	
Fe-2:1					
TES15					

BET surface areas of 182.15 and 181.65 m $^2/g$ were observed for the samples containing either the maximum loading of Fe-NP (US30,BC:Fe-1:1,TES5) or TES (US30,BC:Fe-2:1,TES15). The SEM images also demonstrate the increased partial coating of biochar surface with TES and a uniform distribution of Fe-NP on BC surface (Fig. 3d-f). EDX analysis of the biochar surface (Fig. 3g-h) shows the elemental percentage composition of C, O, Fe and Si on the surfaces of magnetized and magnetized-functionalized biochar. Before TES treatment, Fe from the nanoparticles is detected. After TES, the Si that coats the nanoparticles is detected instead.

3.2.1. Effect of physicochemical magnetization on elemental composition of Biochar

Table 2 lists the elemental (C, H, N, S, O and Fe) and ash contents of raw and double layer magnetized/functionalized biochar composites. As observed, the ultrasound activation of biochar increases the C content of biochar, which is consistent with our previous works. Ultrasound cavitation and its implications (e.g. micro-jets, hot spots, shock waves, etc.) can exfoliate the graphitic structure of biochar and facilitate the leaching of mineral compounds (ash content), which subsequently increases the portion of organic compounds in the biochar structure. In addition, the results show that ultrasound activation slightly reduced the oxygen content of biochar, presumably through the removal of some of the oxygen-containing functional groups [25,26].

Upon magnetization and loading of Fe_3O_4 nanoparticles, the Fe and O contents of the samples increased as expected. Ultrasound activation also affects the loading of Fe_3O_4 nanoparticles. As observed, unsonicated USO,BC:Fe 2:1,TES 5 contained the least Fe (3.8 %) content of the magnetized samples. However, ultrasonication increased the Fe content to 7.93 % and 6.56 % for US30,BC:Fe 2:1,TES5 and US60,BC:Fe2:1, TES5, respectively. Compared to the sonicated-magnetized BC samples, US0,BC:Fe 2:1,TES5 compensated for its low %Fe with a higher quantity of C, H, and N. The higher porosity and surface area of the sonicated samples allows the subsequent incorporation of a higher quantity of FeNP into the biochar structure, which lowers the % of other elements.

As expected, increasing the ratio of BC to magnetic nanoparticles reduced their loading and hence %O declined. However, Fe content showed an increase, which is against our expectations. It should be explained that different combustion analyzers, and therefore different samples, are used for the analysis of C, H, N, S, O; and Fe. This paradox between the O and Fe trends could be due to the agglomeration of nanoparticles in some samples [24]. To probe such paradoxes, we synthesized three sets of samples and analyzed the elements three times.

The last section of the table focuses on the effect of TES concentration during the process of functionalization. As observed, N and ash contents significantly increased with TES concentration from 5 to 15 mL/L. The maximum N content was observed for US 30,BC:Fe 2:1,TES15.

3.2.2. Effect of physiochemical magnetization on functional groups of Biochar

The effects of magnetization and TES functionalization on functional groups of double layer biochar composites under different conditions, as indicated by their FTIR spectra, are provided in Fig. 4. Data were analyzed by Origin software (Figs. 1-3 Supplementary). The wide band at 3300–3600 \mbox{cm}^{-1} represents the stretching vibration of the hydrogenbonded hydroxyl group [36]. The intensification of this bond was significantly reduced due to ultrasound activation, most likely due to the loss of OH and COOH functional groups. This is consistent with our elemental analysis which confirms the reduction of O and H containing groups and our previous studies. According to the literature, the most prominent features of TES are located between 740-1250 cm⁻¹ [37–39]. Accordingly, the characteristic peak at 765–795 cm⁻¹ corresponds to the Si-C vibration [39,40] or SiO-C [41], suggesting that the organic alkyl chains are covalently bonded to the Si-O-Si networks [40, 42]. The other two peaks at 952 cm⁻¹ and 1110 cm⁻¹ were assigned to the Si-O-C bond [39-41] and Si-O-Si stretching [40,43,41], respectively

 Table 2

 Elemental Analysis of raw and activated biochars.

Sample	Carbon (% w/w)	Hydrogen (%w/w)	Nitrogen (%w/w)	Sulfur (%w/w)	Oxygen (%w/w)	Ash (%w/w)	Iron (% w/w)
Raw-BC	60.26	2.96	0.25	0.82	10.79	23.45	0.616
US 30-BC	66.56	2.32	0.21	0.61	9.93	21.20	0.438
US 0, BC:Fe 2:1,TES5	58.75	2.70	0.65	0.70	13.17	22.20	3.80
US 30,BC:Fe 2:1,TES5	54.65	2.24	0.51	0.62	12.59	21.42	7.98
US 60,BC:Fe 2:1,TES5	52.09	1.59	0.56	0.48	12.33	23.00	6.56
US 30,BC:Fe 1:1,TES5	57.42	2.18	0.75	0.87	12.92	22.60	7.33
US 30,BC:Fe 2:1,TES5	54.65	2.24	0.51	0.62	12.59	21.42	7.98
US 30,BC:Fe 3:1,TES5	54.00	2.07	0.49	0.52	12.31	24.52	9.01
US 30,BC:Fe 2:1,TES5	54.65	2.24	0.51	0.62	12.59	21.42	7.98
US 30,BC:Fe 2:1,TES10	57.60	2.09	0.70	0.47	12.21	23.40	8.62
US 30,BC:Fe 2:1,TES15	58.52	2.64	0.79	0.61	12.82	24.65	8.23

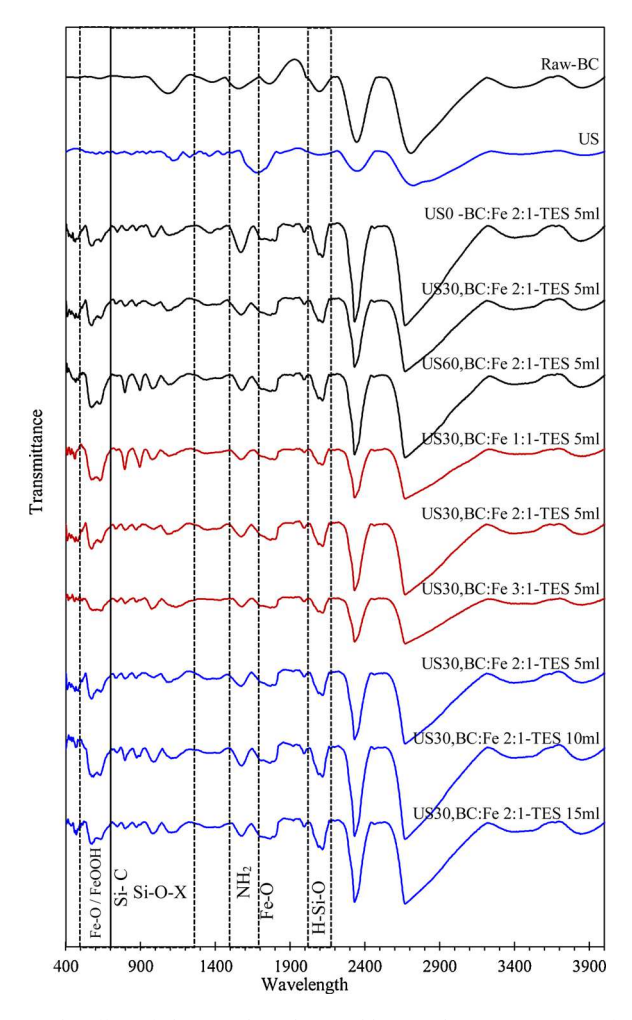


Fig. 4. The effect of ultrasound irradiation (blue) on the FTIR spectrum of raw (black) biochar. The effect of varying ultrasound durations (black) on ultrasound-magnetized biochar. The effect of varying biochar-to-Fenanoparticles ratios (red). The effect of varying TES concentrations (blue).

(herein referred to as the Si-O-X region). These two peaks can confirm the coating of the magnetite surface through the silanization reaction, with hydrolysis of Et-O-Si bonds to make horizontal Si-O-Si links between TES groups (Fig. 2b). The silica network is adsorbed on the surface by Si-O-C bonds (Fig. 1) [41,44].

The peak at $1100~\rm cm^{-1}$ is associated with either the stretching vibration of C—O bonds in the BC structure, C—N of the incorporated C-NH $_2$ bond [39] or Si-O-C or Si-O-Si bonds [45]. The observed Si-corresponding bands prove that TES was successfully grafted onto the magnetized biochar. The other new peak exhibited at $1580-1620~\rm cm^{-1}$

was assigned to the N—H bending of the NH_2 amine group [45,41]. The peak around 2100 cm⁻¹ is likely an overtone of the 1050 region, and the peak at 2300 cm⁻¹ is CO_2 . There could be some overlap between the peaks. As an instance, a peak that is observed 1047 cm⁻¹ could also be associated with Si-O-Fe stretching vibrations [42]. In addition, the two peaks valued at 1635 and 575 cm⁻¹ are assigned to symmetrical and anti-symmetrical Fe–O vibrations [42,46,47] and a small peak next to it (at around 665 cm⁻¹) can result from the FeOOH stretching vibration, which usually appears in activated carbon modified by Fe^{3+} [48,49]. It may also have some overlap with O-Si-O asymmetric flexing [50]. The presence of these two strong bonds in all magnetized samples suggests the attachment of magnetic nanoparticles to the biochar.

Upon magnetization and functionalization, the intensity of Fe-O (575 $\rm cm^{-1})$ and Si-O-X (700–1200 peaks $\rm cm^{-1})$ significantly increased. Among the first group of peaks which reflects the effect of structural modification using ultrasound irradiation, the highest intensities of these peaks were observed for the highest duration of ultrasound activation.

The FTIR spectra of magnetization using different loadings of Fe $_3$ O₄ nanoparticles are represented in maroon color in Fig. 4. As expected, the highest Fe-O peak (at 575 cm $^{-1}$) was observed for US30-BC:Fe 1:1-TES, since an equal quantity of biochar and Fe nanoparticles were used in the activation process. The intensity of this peak gradually decreased with the reduction of Fe-NP loading. Another important observation is that not only Fe-O peak but also the Si-O-X peaks were significantly higher in US30-BC:Fe 1:1-TES5, which can be due to the increased attachment of TES into this sample. However, it does not necessarily improve the adsorption capacity of biochar, as this capability is a resultant of a combination of phenomena including physical adoption, surface complexation, inner-sphere complexation, etc. Higher Fe and TES loading reduces the surface area and porosity of biochar which may negatively affect its adsorption capacity.

The lines highlighted in the blue color of Fig. 4 demonstrate the effect of different TES concentrations in the amination step. The intensity of FTIR peaks of Si-O-X and Fe-O increased with TES concentration up to 10 mL; however, no further increase in the intensity of peaks was observed for the higher TES dose of 15 mL, which is consistent with the trend of Fe and N contents in the samples.

3.2.3. Effect of physiochemical magnetization on graphitic structure of Biochar

Fig. 5a shows the Raman Spectra of the biochars activated and functionalized under different ultrasound irradiation and TES loading. The spectra were recorded with a linear laser excitation of 532 nm and the baselines were revised. In general, their spectra share common features at around 1000–1529, 1500–1775, and 2800 cm⁻¹, the so-called D, G, and 2D peaks respectively. The D-band (or "disorder-induced" peak) is attributed to in-plane vibrations of sp²-bonded carbon within structural defects, amorphous or disordered graphite. The D band has a low intensity in well-organized carbonaceous materials and graphite. However, it becomes similar in intensity to the G band for

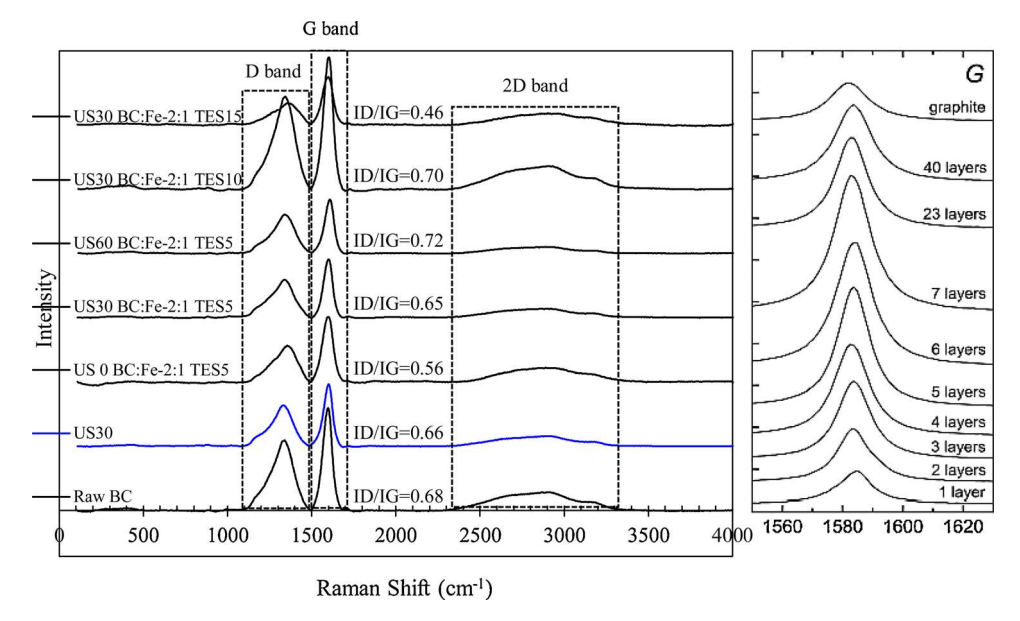


Fig. 5. (a) (Left) Raman Spectra of the biochars activated and functionalized with 2:1 BC:NP under different ultrasound durations and TES loadings. (b) (Right) Evolution of the G band in the Raman spectrum as a function of the number of graphene layers, [47]. Reproduced with copyright license.

more disordered carbons such as biochar. The G-band (stretching carbon-carbon sp 2 bonds) arises from the in-plane vibrations of the sp 2 -bonded carbon in graphitic crystallites. The intensity ratio between the D and G band ($I_{\rm D}/I_{\rm G}$) is a measure of defects in graphite-based materials. The comparable intensity of D-band and G-band with an intensity ratio ranging from 0.46 to 0.72 indicates that biochar is made of a high quantity of ordered and disordered graphitic carbons.

The 2D-band (also known as G'-band) is the second-order overtone of the D-band and is the result of a two phonon lattice vibrational process, but unlike the D-band, it does not need to be activated by proximity to a defect. The 2D band is usually used to determine graphene layer thickness. It is much sharper and more intense in the single-layer graphene than in multi-layer graphene. According to the Raman results and as expected, the biochar structure involves mainly multi-layer graphene (graphitic structure).

It has been reported that the intensity of the G band increases with the number of graphene layers (for thin samples) up to 7 layers, and then decreases with the further increase of the number of layers ($\sim\!23,\,\sim\!40$ layers and graphite, Fig. 5b) [51]. Raw chars usually contain clusters of 4–6 parallel graphene and graphitic oxide sheets [52,53]. Therefore, reduced intensity of G peak can also be related to the exfoliation and reduction of biochar layers due to ultrasound activation. In addition, a lower intensity of D and G bands in ultrasound-activated sample US30 can indicate that the size of the crystallites decreases. This is consistent with our observation confirming the reduced biochar's particle size upon ultrasound activation. The intensity of D and G peaks decreased upon magnetization and functionalization, without ultrasonication. This indicates an increasing roughness and thickness of crystals due to the partial coating of the surface. However, the intensity of the $I_{\rm D}/I_{\rm G}$ ratio increased with ultrasound activation duration from 0.56 for US0-BS: Fe-2:1-TES5 to 0.72 for US60-BS:Fe-2:1-TES5, and was greatest with the lowest TES dosage of 5 mL.

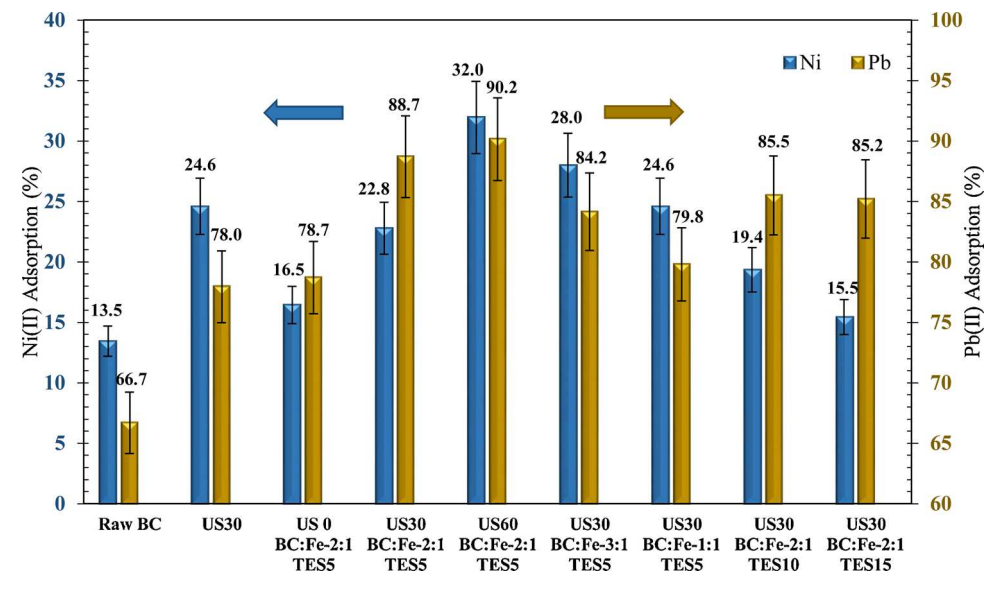


Fig. 6. The effect of ultrasound activation, magnetization and TES functionalization on adsorption of Ni²⁺ and Pb²⁺ by biochar within 6 h.

3.3. Heavy metal adsorption studies

3.3.1. Ultrasound activation effect

Fig. 6 presents the performances of raw and the double layer magnetized/functionalized biochar composite in adsorption of nickel and lead ions. All adsorption tests were conducted two times. As observed, raw biochar can remove only 14 % of nickel and 67 % of lead ions. Generally, the removal of Pb²⁺ ions in aqueous solution is easier than Ni²⁺ ions [54]. The ionic radius, electronegativity (covalent bond strength) and the hydration properties of the metal ions are the principal properties used in the interpretation of heavy metal adsorption mechanisms [55]. Structures with a smaller hydrated radius and higher electronegativity have more potential for surface complexation or adsorption reactions [55]. The degree of hydration of metal ions depends on the ratio of charge (electrostatic charge) to volume. A lower number of water molecules hydrate the larger ions that have smaller charges per volume. Pb(II) ions have a larger ionic radius than Ni(II) ions (0.119 vs 0.069 nm); however, the hydrated radius of Pb(II) ions is smaller than that of Ni(II) ions (0.401 nm vs 0.404 nm) [56]. The ion with the smaller hydrated radius should be adsorbed more strongly. On the other hand, stronger covalent bonds should be formed with more electronegative metals; lead (2.33) is more electronegative than nickel (1.91). The combination of higher electronegativity and a smaller hydration radius ensures a higher covalent bond between the lead ion and the electron donor of the adsorbent surface, compared to nickel [54,57].

Short term physical activation of biochar with ultrasound irradiation increased the nickel removal to 25 % and lead removal to 78 %. This improvement was caused by the ultrasound cavitation and its implications which subsequently increased the surface area and porosity of BC. Additionally, micro-jets can generate new pores and open some of the blocked pores which not only increases the porosity of biochar but also makes channels to the underlayers of biochar where some functional groups are secluded. These effects also favor the magnetization and functionalization steps.

Magnetization usually decreases the adsorption capacity of biochar. However, comparing the adsorption results of USO-BC:Fe 2:1-TES5 to raw BC demonstrates the contribution of amine functionalization following magnetization, which not only prevented overall reduction of metal removal but even slightly increased the adsorption capacity of biochar. Ultrasound activation of biochar prior to magnetization and functionalization further increased the metal removal. Given the fact that the maximum nickel and lead removal without ultrasound was 17 % and 79 % (for USO-BC:Fe 2:1-TES5), a significant increase of Ni and Pb adsorption (to 32 % and 90 % respectively for US60-BC:Fe 2:1-TES5) is attributed to the structural modification accompanying ultrasound irradiation.

3.3.2. Magnetization effect

The magnetization process was conducted using three different BC: Fe ratios of 1:1, 2:1, and 3:1. For nickel, the lowest the nanoparticle loading corresponded to the greatest the adsorption capacity. The reduction of biochar's adsorption capacity with nanoparticle loading is mainly due to the nanoparticles reducing the surface area and the porosity of biochar. Therefore, among the three Fe₃O₄ loadings with 30 s of ultrasound pre-activation, the maximum Ni(II) adsorption of 28 % was observed for US30-BC:Fe 3:1-TES5, which contained the lowest quantity of Fe₃O₄ nanoparticles. The value further increased to 32 % for longer ultrasonication (US60-BC:Fe 3:1-TES5). Moreover, longer ultrasound activation significantly reduced the adsorption time (increased the adsorption rate, in other words) (Fig. S2). The highest amount of nickel was removed by US60-BC:Fe 3:1-TES5 within only 2 h. In terms of lead removal, the highest absorption was observed for US30-BC:Fe 2:1-TES5 rather than for US30-BC:Fe 3:1-TES5. However, in this case, the sample containing the highest Fe-NP loading (US30-BC:Fe 1:1-TES5) displayed the least adsorption.

3.3.3. Functionalization effect

Among samples with US30 and 2:1 BCE:Fe loading, the highest adsorption of both Ni(II) and Pb(II) was observed for the sample containing the lowest TES loading, US30-BC:Fe2:1-TES5. Further increasing the TES concentration reduced the adsorption capacity of the activated biochars. This can be due to the significant impact of chemical functionalization in reducing the surface area and porosity of adsorbent, particularly in terms of Ni(II) adsorption. However, the contradictory impact of TES in increasing the removal of Pb(II) can be noticed by comparing the results of US30 (78 %) and US30-BC:Fe 2:1-TES5 (89 %). It is worth noting to mention that this project was initially conducted by direct precipitation of Fe₃O₄ on the USBC surface without any functionalization (not covered in the manuscript), which caused a significant reduction in the adsorption capacity of biochar. This could be mainly due to the reduction in surface area and porosity of biochar. However, it also suggested that Fe₃O₄ did not make a significant contribution to the adsorption process. Therefore, the increase in adsorption capacity of TES functionalized magnetic-USBC suggests a determinant role of chemisorption by the amino groups of TES in Pb removal. Such a prominent capability of TES in removal of lead and other heavy metals has also been reported by other researchers [58]. For example, Kong et al. [59] functionalized the surface of silica nanoparticles by three silane coupling agents, including 3-mercaptopropyltriethoxysilane (MPTES) and TES, and compared their performances on the removal of Pb(II), Cu (II), Hg(II), Cd(II), and Zn(II). TES-functionalized silica nanoparticles (SiO₂-TES) exhibited maximum removal efficiency towards Pb²⁺ and Hg²⁺. Shi et al. [60] also synthesized magnetic biochar in three steps, including preparation of carboxylated biochar, synthesis of Fe₃O₄@-SiO₂-NH₂ particles from Fe₃O₄ particles modified with TEOS and TES via the "Stober" method, and then conjugation of the Fe₃O₄@SiO₂-NH₂ with the carboxylated biochar by forming amide bonds via the classic EDC-NHS coupling. The Cr(VI) ion adsorption capacity of their magnetic biochar was 27.2 mg g⁻¹, surpassing the original carboxylated biochar (18.2 mg g⁻¹). Compared to their work, the method developed in this study is much simpler. In addition, the focus of the current work is promoting the adsorption and functionalization capability of biochar rather than using it as a carrier or support. And the final difference of this study over the other similar works is that pH as a master variable in adsorption of heavy metals was not adjusted in this study and the adsorption was conducted on the inherent pH of the solution.

3.4. Kinetic and the equilibrium adsorption

Based on the analysis presented in Figs. S2-S3 and Tables S1-S2 (Supplementary Information), the pseudo-second-order model was generally more suitable for explaining the behavior of Pb(II) adsorption into magnetized biochar, indicating that the reaction is more inclined towards chemisorption due to the impact of functional groups on biochar surface rather than physisorption. The pseudo-second-order plots were also superior for Ni(II) adsorption. However, the pseudo-first-order plots also showed reasonable R values (> 0.9) for 2/3 of the sonicated Ni samples, suggesting an impact for both physisorption and chemisorption in Ni removal. However, most of the metal removal was accomplished during the early stage of adsorption, 30 min out of 6 h. The difference between the calculated and experimental values of adsorption capacities, shows that a more number of data points is needed from during the early stages of adsorption.

4. Conclusion

This study introduced a post-pyrolysis ultrasound-based magnetization process to produce the double layer magnetic/ TES functionalized biochar. According to FTIR analysis, the most prominent features of TES are located between $740-1250~{\rm cm}^{-1}$ (Si-C vibration, Si-O-C peak and Si-O-Si stretching), which can confirm the coating of the magnetite surface through the silanization reaction and the formation of silica

network on the BC surface by Si-O-C bonds. The adsorption results demonstrated that while raw biochar could remove only 13 % and 68 % of Ni(II) and Pb(II), with some signs of leaching, the biochar activated under 60 s of ultrasound irradiation, magnetized with Fe₃O₄ in the ratio of 2:1, and functionalized with the lowest concentration of TES exhibited 32 % and 90 % of Ni and Pb removal, without any leaching. The highest adsorption capacity was associated with the maximum ultrasound activation of 60 s, which suggests the impact of porosity and surface area on the subsequent functionalization and the removal of metal ions. Although the low concentration of TES increased the adsorption capacity, high TES concentrations adversely affected the adsorption capacity, due to the reduction of surface area and Porosity. Kinetic studies suggest that Pb(II) adsorption is more inclined towards chemisorption, while both physisorption and chemisorption contribute to Ni removal. The bulk of the biochar could be separated from water by application of a neodymium magnet, even at the lowest Fe-NP loading of BC:Fe = 3:1, indicating facile removal of metal ion contaminants from solution with magnetized-functionalized biochar composite.

Declaration of Competing Interest

The authors declare that they have no conflict of interest.

Acknowledgements

The authors are grateful for the financial support of the National Science Foundation (NSF EPSCoR RII Grant No. OIA-1632899 and MRI Grant No. CHE-1532079) of the United States. The author also appreciates the UM Science, Technology, Engineering, and Math Summer Research Experience for Undergraduates (STEMS REU) Program at the University of Mississippi.

Appendix A. Supplementary data

Supplementary material related to this article can be found, in the online version, at doi:https://doi.org/10.1016/j.jwpe.2020.101677.

References

- [1] M.A. Barakat, New trends in removing heavy metals from industrial wastewater, Arab. J. Chem. 4 (4) (2011) 361–377.
- [2] S. Cobbina, A. Duwiejuah, R. Quansah, S. Obiri, N. Bakobie, Comparative Assessment of Heavy Metals in Drinking Water Sources in Two Small-Scale Mining Communities in Northern Ghana., Vol. 12, 2015, pp. 10620–10634.
- [3] S. Babel, T.A. Kurniawan, Cr(VI) removal from synthetic wastewater using coconut shell charcoal and commercial activated carbon modified with oxidizing agents and/or chitosan, Chemosphere 54 (7) (2004) 951–967.
- [4] B. Sajjadi, W.-Y. Chen, N.O. Egiebor, A comprehensive review on physical activation of biochar for energy and environmental applications, Rev. Chem. Eng. 35 (6) (2019) 735–776.
- [5] A.H. Fahmi, A.W. Samsuri, H. Jol, D. Singh, Physical modification of biochar to expose the inner pores and their functional groups to enhance lead adsorption, RSC Adv. 8 (67) (2018) 38270–38280.
- [6] L. Leng, S. Xu, R. Liu, T. Yu, X. Zhuo, S. Leng, Q. Xiong, H. Huang, Nitrogen containing functional groups of biochar: an overview, Bioresour. Technol. 298 (2020), 122286.
- [7] B. Sajjadi, T. Zubatiuk, D. Leszczynska, J. Leszczynski, W.Y. Chen, Chemical activation of biochar for energy and environmental applications: a comprehensive review, Rev. Chem. Eng. 35 (2018) 777–815.
- [8] A.G. Karunanayake, O.A. Todd, M. Crowley, L. Ricchetti, C.U. Pittman, R. Anderson, D. Mohan, T. Mlsna, Lead and cadmium remediation using magnetized and nonmagnetized biochar from Douglas fir, Chem. Eng. J. 331 (2018) 480–491.
- [9] X. Li, C. Wang, J. Zhang, J. Liu, B. Liu, G. Chen, Preparation and application of magnetic biochar in water treatment: a critical review, Sci. Total Environ. 711 (2020), 134847.
- [10] Y. Yi, Z. Huang, B. Lu, J. Xian, E.P. Tsang, W. Cheng, J. Fang, Z. Fang, Magnetic biochar for environmental remediation: a review, Bioresour. Technol. 298 (2020), 122468
- [11] M.M. Mian, G. Liu, B. Yousaf, B. Fu, H. Ullah, M.U. Ali, Q. Abbas, M.A. Mujtaba Munir, L. Ruijia, Simultaneous functionalization and magnetization of biochar via NH3 ambiance pyrolysis for efficient removal of Cr (VI), Chemosphere 208 (2018) 712–721.

- [12] Z. Liu, F.-S. Zhang, R. Sasai, Arsenate removal from water using Fe3O4-loaded activated carbon prepared from waste biomass, Chem. Eng. J. 160 (1) (2010) 57–62
- [13] M. Zahoor, F. Ali Khan, Adsorption of aflatoxin B1 on magnetic carbon nanocomposites prepared from bagasse, Arab. J. Chem. 11 (5) (2018) 729–738.
- [14] A.S. Liyanage, S. Canaday, C.U. Pittman, T. Mlsna, Rapid remediation of pharmaceuticals from wastewater using magnetic Fe3O4/Douglas fir biochar adsorbents, Chemosphere 258 (2020), 127336.
- [15] B. Chen, Z. Chen, S. Lv, A novel magnetic biochar efficiently sorbs organic pollutants and phosphate, Bioresour. Technol. 102 (2) (2011) 716–723.
- [16] Z. Zhou, Y.-g. Liu, S.-b. Liu, H.-y. Liu, G.-m. Zeng, X.-f. Tan, C.-p. Yang, Y. Ding, Z.-l. Yan, X.-x. Cai, Sorption performance and mechanisms of arsenic(V) removal by magnetic gelatin-modified biochar, Chem. Eng. J. 314 (2017) 223–231.
- [17] K.R. Thines, E.C. Abdullah, N.M. Mubarak, M. Ruthiraan, Synthesis of magnetic biochar from agricultural waste biomass to enhancing route for waste water and polymer application: a review, Renewable Sustainable Energy Rev. 67 (2017) 257–276.
- [18] M. Zhang, B. Gao, S. Varnoosfaderani, A. Hebard, Y. Yao, M. Inyang, Preparation and characterization of a novel magnetic biochar for arsenic removal, Bioresour. Technol. 130 (2013) 457–462.
- [19] D. Mohan, P. Singh, A. Sarswat, P.H. Steele, C.U. Pittman, Lead sorptive removal using magnetic and nonmagnetic fast pyrolysis energy cane biochars, J. Colloid Interface Sci. 448 (2015) 238–250.
- [20] K. Philippou, I. Anastopoulos, C. Dosche, I. Pashalidis, Synthesis and characterization of a novel Fe3O4-loaded oxidized biochar from pine needles and its application for uranium removal. Kinetic, thermodynamic, and mechanistic analysis, J. Environ. Manage. 252 (2019), 109677.
- [21] M. Gazi, A.A. Oladipo, K.A. Azalok, Highly efficient and magnetically separable palm seed-based biochar for the removal of nickel, Sep. Sci. Technol. 53 (7) (2018) 1124–1131.
- [22] Y. Zhao, R. Zhang, H. Liu, M. Li, T. Chen, D. Chen, X. Zou, R.L. Frost, Green preparation of magnetic biochar for the effective accumulation of Pb(II): Performance and mechanism, Chem. Eng. J. 375 (2019), 122011.
- [23] Q. Cui, J. Xu, W. Wang, L. Tan, Y. Cui, T. Wang, G. Li, D. She, J. Zheng, Phosphorus recovery by core-shell γ-Al2O3/Fe3O4 biochar composite from aqueous phosphate solutions, Sci. Total Environ. 729 (2020), 138892.
- [24] J. Alchouron, C. Navarathna, H.D. Chludil, N.B. Dewage, F. Perez, E.B. Hassan, C. U. Pittman Jr, A.S. Vega, T.E. Mlsna, Assessing South American Guadua chacoensis bamboo biochar and Fe3O4 nanoparticle dispersed analogues for aqueous arsenic (V) remediation, Sci. Total Environ. 706 (2020), 135943.
- [25] W.-Y. Chen, D.L. Mattern, E. Okinedo, J.C. Senter, A.A. Mattei, C.W. Redwine, Photochemical and acoustic interactions of biochar with CO₂ and H₂O: applications in power generation and CO₂ capture, Aiche J. 60 (3) (2014) 1054–1065.
- [26] B. Sajjadi, W.-Y. Chen, A. Adeniyi, D.L. Mattern, J. Mobley, C.-P. Huang, R. Fan, Variables governing the initial stages of the synergisms of ultrasonic treatment of biochar in water with dissolved CO₂, Fuel 235 (2019) 1131–1145.
- [27] R. Chatterjee, B. Sajjadi, D.L. Mattern, W.-Y. Chen, T. Zubatiuk, D. Leszczynska, J. Leszczynski, N.O. Egiebor, N. Hammer, Ultrasound cavitation intensified amine functionalization: a feasible strategy for enhancing CO₂ capture capacity of biochar, Fuel 225 (2018) 287–298.
- [28] S. Singh, G. Singh, N. Bala, K. Aggarwal, Characterization and preparation of Fe3O4 nanoparticles loaded bioglass-chitosan nanocomposite coating on Mg alloy and in vitro bioactivity assessment, Int. J. Biol. Macromol. 151 (2020) 519–528.
- [29] H. Bamdad, K. Hawboldt, S. MacQuarrie, Nitrogen functionalized biochar as a renewable adsorbent for efficient CO2 removal, Energy Fuels 32 (11) (2018) 11742–11748.
- [30] L. Russo, F. Taraballi, C. Lupo, A. Poveda, J. Jimenez-Barbero, M. Sandri, A. Tampieri, F. Nicotra, L. Cipolla, Carbonate hydroxyapatite functionalization: a comparative study towards (bio)molecules fixation, Interface Focus 4 (1) (2014), 20130040.
- [31] R. Chatterjee, B. Sajjadi, W.-Y. Chen, D.L. Mattern, N. Hammer, V. Raman, A. Dorris, Effect of Pyrolysis Temperature on PhysicoChemical Properties and Acoustic-Based Amination of Biochar for Efficient CO2 Adsorption, Front. Energy Res. 8 (85) (2020).
- [32] A. Houshmand, W.M.A. Wan Daud, M.S. Shafeeyan, Exploring potential methods for anchoring amine groups on the surface of activated carbon for CO₂ adsorption, Sep. Sci. Technol. 46 (7) (2011) 1098–1112.
- [33] D. Chen, H. Zhang, K. Yang, H. Wang, Functionalization of 4-aminothiophenol and 3-aminopropyltriethoxysilane with graphene oxide for potential dye and copper removal, J. Hazard. Mater. 310 (2016) 179–187.
- [34] S.E. Cabaniss, Forward modeling of metal complexation by NOM: II. Prediction of binding site properties, Environ. Sci. Technol. 45 (8) (2011) 3202–3209.
- [35] S.-S. Kim, M.J. Park, J.-H. Kim, G. Ahn, S. Ryu, B.H. Hong, B.-H. Sohn, Strain-assisted wafer-scale nanoperforation of single-layer graphene by arrayed pt nanoparticles, Chem. Mater. 27 (20) (2015) 7003–7010.
- [36] S. Knop, T.L.C. Jansen, J. Lindner, P. Vöhringer, On the nature of OH-stretching vibrations in hydrogen-bonded chains: pump frequency dependent vibrational lifetime, J. Chem. Soc. Faraday Trans. 13 (10) (2011) 4641–4650.
- [37] T. Zhou, X. Zhao, S. Wu, L. Su, Y. Zhao, Efficient capture of aqueous humic acid using a functionalized stereoscopic porous activated carbon based on poly(acrylic acid)/food-waste hydrogel, J. Environ. Sci. 77 (2019) 104–114.
- [38] S.R. Balakrishnan, U. Hashim, S.C. Gopinath, P. Poopalan, H.R. Ramayya, P. Veeradasan, R. Haarindraprasad, A.R. Ruslinda, Polysilicon nanogap lab-on-chip facilitates multiplex analyses with single analyte, Biosens. Bioelectron. 84 (2016) 44–52.

- [39] P.A. Ling, H. Ismail, Tensile Properties, Water Uptake, and Thermal Properties of Polypropylene/Waste Pulverized Tire/Kenaf (PP/WPT/KNF) Composites, Vol. 8, 2012, 2012.
- [40] F. Cui, T. Cui, Self-catalytic synthesis of metal oxide nanoclusters@mesoporous silica composites based on successive spontaneous reactions at near neutral conditions, Chem. Commun. 50 (94) (2014) 14801–14804.
- [41] J. Vieillard, N. Bouazizi, R. Bargougui, N. Brun, P. Fotsing Nkuigue, E. Oliviero, O. Thoumire, N. Couvrat, E. Djoufac Woumfo, G. Ladam, N. Mofaddel, A. Azzouz, F. Le Derf, Cocoa shell-deriving hydrochar modified through aminosilane grafting and cobalt particle dispersion as potential carbon dioxide adsorbent, Chem. Eng. J. 342 (2018) 420–428.
- [42] S. Shi, J. Yang, S. Liang, M. Li, Q. Gan, K. Xiao, J. Hu, Enhanced Cr(VI) removal from acidic solutions using biochar modified by Fe3O4@SiO2-NH2 particles, Sci. Total Environ. 628-629 (2018) 499–508.
- [43] R.M. Pasternack, S. Rivillon Amy, Y.J. Chabal, Attachment of 3-(Aminopropyl) triethoxysilane on silicon oxide surfaces: dependence on solution temperature, Langmuir. 24 (22) (2008) 12963–12971.
- [44] S.M. Salili, A. Ataie, M.R. Barati, Z. Sadighi, Characterization of mechanothermally synthesized Curie temperature-adjusted La0.8Sr0.2MnO3 nanoparticles coated with (3-aminopropyl) triethoxysilane, Mater. Charact. 106 (2015) 78–85.
- [45] N. Majoul, S. Aouida, B. Bessaïs, Progress of porous silicon APTESfunctionalization by FTIR investigations, Appl. Surf. Sci. 331 (2015) 388–391.
- [46] J.Y. Lim, N.M. Mubarak, M. Khalid, E.C. Abdullah, N. Arshid, Novel fabrication of functionalized graphene oxide via magnetite and 1-butyl-3-methylimidazolium tetrafluoroborate, Nano-structures Nano-objects 16 (2018) 403–411.
- [47] W. Wei, W. Sun, H. Hu, Z. Jiang, L. Ma, J. Xie, Controllable synthesis of magnetic Fe3O4 encapsulated semimetal Bi nanospheres with excellent stability and catalytic activity, J. Mater. Sci. 53 (19) (2018) 13886–13899.
- [48] Y. Liu, X. Liu, W. Dong, L. Zhang, Q. Kong, W. Wang, Efficient adsorption of sulfamethazine onto modified activated carbon: a plausible adsorption mechanism, Sci. Rep. 7 (1) (2017) 12437.
- [49] X.N. Pham, T.P. Nguyen, T.N. Pham, T.T.N. Tran, T.V.T. Tran, Synthesis and characterization of chitosan-coated magnetite nanoparticles and their application in curcumin drug delivery, Adv. Nat. Sci. Nanosci. Nanotechnol. 7 (4) (2016), 045010

- [50] Z. Huang, P. Wu, B. Gong, Y. Dai, P.-C. Chiang, X. Lai, G. Yu, Efficient removal of Co2+ from aqueous solution by 3-Aminopropyltriethoxysilane functionalized montmorillonite with enhanced adsorption capacity, PLoS One 11 (7) (2016), e0159802.
- [51] D. Yoon, H. Moon, H. Cheong, J.S. Choi, J.A. Choi, B.H. Park, Variations in the raman Spectrum as a function of the number of graphene layers, J. Korean Phys. Soc. 55 (3) (2008) 1299–1303.
- [52] R.E. Franklin, Crystallite growth in graphitizing and non-graphitizing carbons, Proc. R. Soc. Lond. A Math. Phys. Sci. 209 (1097) (1951) 196–218.
- [53] K. Hammes, M.W.I. Schmidt, Changes of biochar in soil, in: J. Lehmann, S. Joseph (Eds.), Biochar for Environmental Management, Science and Technolog, EarthScan., United Kingdom, 2009.
- [54] J.P. Holmberg, Competitive Adsorption and Displacement Behaviour of Heavy Metals on Peat in Department of Civil and Environmental Engineering, Chalmers University of Technology, 2006.
- [55] W. Zhan, C. Xu, G. Qian, G. Huang, X. Tang, B. Lin, Adsorption of Cu(ii), Zn(ii), and Pb(ii) from aqueous single and binary metal solutions by regenerated cellulose and sodium alginate chemically modified with polyethyleneimine, RSC Adv. 8 (33) (2018) 18723–18733.
- [56] E.R. Nightingale, phenomenological theory of ion solvation. Effective radii of hydrated ions, J. Phys. Chemi. 63 (9) (1959) 1381–1387.
- [57] P.R. Puranik, K.M. Paknikar, Influence of co-cations on biosorption of lead and zinc – a comparative evaluation in binary and multimetal systems, Bioresour. Technol. 70 (3) (1999) 269–276.
- [58] S. Tang, N. Shao, C. Zheng, F. Yan, Z. Zhang, Amino-functionalized sewage sludgederived biochar as sustainable efficient adsorbent for Cu(II) removal, Waste Manag. 90 (2019) 17–28.
- [59] X.-f. Kong, B. Yang, H. Xiong, Y. Zhou, S.-g. Xue, B.-q. Xu, S.-x. Wang, Selective removal of heavy metal ions from aqueous solutions with surface functionalized silica nanoparticles by different functional groups, J. Cent. South Univ. 21 (9) (2014) 3575–3579.
- [60] S. Shi, J. Yang, S. Liang, M. Li, Q. Gan, K. Xiao, J. Hu, Enhanced Cr(VI) removal from acidic solutions using biochar modified by Fe3O4@SiO2-NH2 particles, Sci. Total Environ. 628-629 (2018) 499–508.